Voigt-effect-based three-dimensional vector magnetometer

Tadas Pyragius,[1] Hans Marin Florez,[1,2] and Thomas Fernholz[1,*]
[1]*School of Physics and Astronomy, University of Nottingham, University Park, Nottingham NG7 2RD, England, United Kingdom*
[2]*Instituto de Física, Universidade de São Paulo, 05315-970 São Paulo, São Paulo, Brazil*

(Received 12 April 2019; revised manuscript received 26 July 2019; published 21 August 2019)

We describe a method to dispersively detect all three vector components of an external magnetic field using alkali-metal atoms based on the Voigt effect. Our method relies on measuring the linear birefringence of the radio-frequency dressed atomic medium via polarization homodyning. This gives rise to modulated polarization signals at the first and second harmonic of the dressing frequency. The vector components of the external magnetic field are mapped onto the quadratures of these harmonics. We find that our scheme can be utilized in both cold and hot atomic gases to detect such external fields in shielded and unshielded environments. In the shielded hot vapor case we achieve field sensitivities in the $\mathrm{pT}/\sqrt{\mathrm{Hz}}$ range for all three vector components, using pump-probe cycles with 125-Hz repetition rate, and limited by the short coherence time of the cell. Finally, our scheme has a simple single axis beam geometry, making it advantageous for miniature magnetic-field sensors.

DOI: 10.1103/PhysRevA.100.023416

I. INTRODUCTION

Optically pumped magnetometers (OPMs) have increasingly been in the spotlight for their broad span of applications ranging from fundamental physics experiments to medical physics. Examples include measurements of the electric dipole moment [1,2] and searches for exotic physics [3] as well as magnetoencephalography [4,5] and magnetocardiography [6–8] where detection of the small magnetic fields of the brain and the heart is required. A review can be found in [9]. In recent years OPMs have become the state-of-the-art magnetic-field sensors achieving sub-$\mathrm{fT}/\sqrt{\mathrm{Hz}}$ sensitivity and surpassing the well-established superconducting quantum interference device based sensors [10–12]. In its simplest operation, an OPM uses a pump-probe laser to measure the atomic Larmor frequency, i.e., the frequency of spin precession, by interacting with optically pumped atoms, which in effect measures the strength of the external magnetic field. However, in a larger range of applications, a complete determination of the magnetic field is required. Some schemes employ a scalar magnetometer to run as a vector magnetometer by applying a rotating low-frequency-bias magnetic field [13,14]. Another possible approach uses multiple radio-frequency modulations to map the three vector components onto the harmonics of the signal [15,16]. The effects of the field orientation on the resulting signal phase have been studied for different configurations of a modulating field and may be used for full vector magnetometry [17]. Also an all-optical scheme with crossed beams was demonstrated to extract the three field components [18]. To date, most of the OPM schemes are based on pump-probe configurations that rely on the Faraday rotation, i.e., circular birefringence of the medium. As a result, the majority of such schemes require an orthogonal pump-probe geometry for high efficiency of detection [10]. However, this geometry is not convenient for developing miniature sensors, while a parallel configuration is compatible with chip-scale and compact atomic magnetometers. The issue can be overcome by introducing modulation fields, but several fields are required to extract the full information.

In this paper we demonstrate an alternative three-dimensional (3D) vector magnetometer based on the measurement of the Voigt effect, i.e., linear birefringence arising from aligned rather than oriented spin states. It is measured with a probe beam detuned from an optical resonance, in the presence of a single radio-frequency field [19]. Previous work on double resonance detection of aligned states measured linear dichroism on a resonant optical transition [20,21]. The method presented here maps the three vector components of the external field, detected via demodulation of the probe beam's ellipticity, onto orthogonal quadratures of the first and second harmonic of the dressing frequency. State preparation and detection are performed in a parallel pump-probe geometry. We demonstrated vector capability of our magnetometer over a range of ± 0.3-nT longitudinal and ± 180-nT transverse fields and analyzed its sensitivity in a shielded environment in open loop operation. Active feedback on the external field should enable an extension of dynamic range as well as operation in unshielded scenarios.

The paper is organized as follows. In Sec. II, we briefly describe the linear birefringence induced by radio-frequency dressed states. This provides predictions for the mapping of field components onto orthogonal quadratures of the first and second harmonics of the rf oscillation in the signal's response. In the following part of the paper, we report on the experimental realization using two different types of atomic ensemble. Section III demonstrates the detection principle with laser cooled atoms, prepared in a pure quantum state. Section IV describes the extension to a magnetically shielded vapor cell by combining the Voigt effect with synchronous

*thomas.fernholz@nottingham.ac.uk

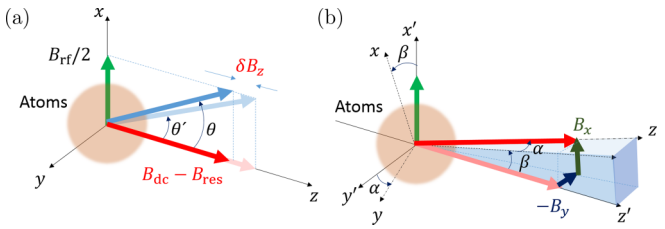

FIG. 1. Geometrical depiction of the effective field in the rotating frame. (a) The effective field encloses an angle θ with the z axis. An external field variation δB_z changes the angle $\theta \to \theta'$. (b) The presence of transverse external fields B_y and B_x also changes the orientation of the effective field, rotating it by angles α and β, respectively.

pumping. Experimental results on vector sensitivity are shown together with an analysis of noise performance. Section V presents our conclusions.

II. MAGNETOMETRY WITH RADIO-FREQUENCY DRESSED STATES

Optically pumped magnetometers utilize dispersive coupling of light to an atomic ensemble in the presence of an external magnetic field. The Larmor precession of spin-polarized atoms causes a modulation of the medium's birefringence, which can be observed polarimetrically. In our scheme, we actively drive such precession with an additional radio-frequency field. Here, we present a brief description of the driven medium and its interaction with the light field in terms of dressed states, as discussed in our previous work [19]. Our model includes the dependence on field orientation, which allows for the extraction of full vector information from measurements of either linear or circular birefringence.

We consider atoms interacting with a static field $\mathbf{B}_{dc} = B_{dc}\mathbf{e}_z$ and a field oscillating at a radio frequency ω in a transverse direction $\mathbf{B}_{rf}(t) = B_{rf}\cos(\omega t)\mathbf{e}_x$. For weak fields, the time-dependent interaction Hamiltonian of an atom with spin $\mathbf{F}$ of constant magnitude can be approximated by $\hat{H} = (\mu_B g_F/\hbar)\hat{\mathbf{F}}\cdot[\mathbf{B}_{rf}(\omega t) + \mathbf{B}_{dc}]$, where μ_B is the Bohr magneton, g_F is the Landé factor, and $\hbar$ is the reduced Planck constant. Depending on the sign of the g_F factor, using positive ω, we transform the Hamiltonian to a frame rotating about the z axis, according to $\hat{H}_{rot} = \hat{U}\hat{H}\hat{U}^{-1} + i\hbar^{-1}(\partial_t\hat{U})\hat{U}^{-1}$ with a time-dependent rotation operator $\hat{U} = e^{\mathrm{sgn}(g_F)i\omega t\hat{F}_z/\hbar}$. Neglecting counter-rotating terms, the transformed effective Hamiltonian takes the form

$$\hat{H}_{eff} = \frac{\mu_B g_F}{\hbar}\hat{\mathbf{F}}\cdot\mathbf{B}_{eff}. \tag{1}$$

The effective magnetic field in this frame is given by $\mathbf{B}_{eff} = B_\rho\mathbf{e}_x + (B_{dc} - B_{res})\mathbf{e}_z$, where $B_\rho = B_{rf}/2$, and $B_{res} = \pm\hbar\omega/\mu_B g_F$ corresponds to a fictitious magnetic field that defines a resonance condition for the Larmor precession [19]. As depicted in Fig. 1(a), the angle enclosed by the effective field and the z axis is

$$\theta = \frac{\pi}{2} - \tan^{-1}\frac{B_{dc} - B_{res}}{B_\rho}. \tag{2}$$

E.g., at resonance, i.e., for $\theta = \pi/2$, the effective field is orthogonal to the static field $\mathbf{B}_{dc}$, pointing in the rotating frame's x direction.

The eigenstates of the effective rotating-frame Hamiltonian, i.e., the dressed states, can be written as $|\Psi_{rot}\rangle = e^{i\theta\hat{F}_y/\hbar}|F, F_z\rangle$, but in the laboratory frame the same states are time dependent, given by $|\Psi(t)\rangle = \hat{U}^{-1}|\Psi_{rot}\rangle$. The dressed states can be prepared directly by synchronous optical pumping [22], or by adiabatic dressing of bare states $|F, F_z\rangle$, which acquire only a time-dependent phase under transformation to the rotating frame, leading to a different (quasi-) energy. In our scheme, magnetometer operation does not rely on a purely dynamical spin evolution, which would be observed as a change in precession frequency. Instead, we assume adiabatic following of dressed states that remain aligned with the effective field. Magnetometry is then enabled by the orientational dependence of the effective field on an additional external field.

An external field in the z direction enters the spin evolution through the dependence of θ on the static field strength [see Eq. (2) and Fig. 1(a)], where we can control the sensitivity $\partial\theta/\partial B_z$ by applying an offset field, such that $B_z = B_{offs} + \delta B_z$. The presence of transverse static fields can also be represented by rotations, as shown in Fig. 1(b). Field components $B_{y,x}$ rotate the static field about the x and y axes by angles α and β, respectively. Hence, using a sequential rotation $\mathbf{M}(\alpha, \beta) = \mathbf{R}_x(\alpha)\mathbf{R}_y(\beta)$ [23], the atomic spin operator in the laboratory frame is given by $\hat{\mathbf{F}}' = \mathbf{M}(\alpha, \beta)\hat{\mathbf{F}}$, where unprimed coordinates are aligned with the actual field. Figure 1 shows that the angles α and β are given by

$$\alpha = \arctan\left(\frac{-B_y}{B_z}\cos(\beta)\right), \tag{3}$$

$$\beta = \arctan\left(\frac{B_x}{B_z}\right), \tag{4}$$

with the small-angle approximation

$$\alpha \approx \frac{-B_y}{B_z},\ \beta \approx \frac{B_x}{B_z}. \tag{5}$$

For a complete description at larger angles, we need to include that the transverse fields increase the actual static field strength to $B_{dc} = \sqrt{B_z^2 + B_x^2 + B_y^2}$, and that the applied rf field is not corotated, leading to a reduction of its effective amplitude in the rotating frame, given by $B_\rho = (B_{rf}/2)\cos\beta$.

For the detection of the spin evolution we employ $+45^\circ$ linearly polarized probe light propagating in the z direction with a corresponding Stokes parameter $S_y = (c/2)\langle\hat{a}_x^\dagger\hat{a}_y + \hat{a}_y^\dagger\hat{a}_x\rangle$, which is equal to half the photon flux [19]. The dispersive interaction of the atomic medium with off-resonant light may lead to both circular and linear birefringence, depending on the atomic spin-dependent polarizability tensor. After propagation through the medium, neglecting absorption and assuming sufficiently small phase angles, the resulting Faraday and Voigt rotation can be described by Stokes operators

$$\langle\hat{S}_x'(t)\rangle = -G_F^{(1)}S_y n_F\langle\hat{F}_z(t)\rangle, \tag{6}$$

$$\langle\hat{S}_z'(t)\rangle = G_F^{(2)}S_y n_F\langle\hat{F}_x^2(t) - \hat{F}_y^2(t)\rangle, \tag{7}$$

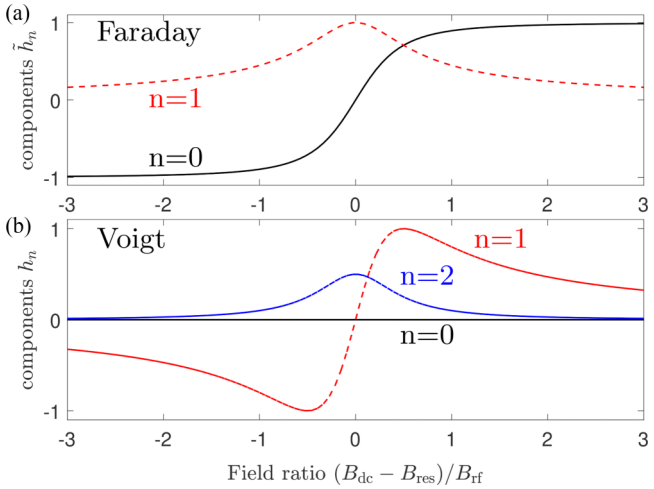

FIG. 2. Spectral decomposition of (a) Faraday rotation proportional to $\langle F_z \rangle$ and (b) Voigt rotation proportional to $\langle F_x^2 - F_y^2 \rangle$, with harmonics $n = 0$ (solid black lines), $n = 1$ (dashed red lines), and $n = 2$ (dash-dotted blue lines).

where $\hat{S}'_z$ and $\hat{S}'_x$ represent the polarization's rotation and ellipticity as photon flux imbalances of the output light, measured in either a circular or a linear basis. The coupling strengths $G_F^{(k)}$ depend on light detuning, the interaction cross section, and the rank-k components of the polarizability tensor. In these equations, we assume interaction with n_F atoms in the same spin state within one hyperfine F manifold and neglect dispersive back-action on the atoms (Stark shifts) [19].

For eigenstates of the effective Hamiltonian, using the geometrical rotations by angles α, β, and θ, we can determine the temporal atomic response in the laboratory frame, measured via Faraday or Voigt effect, in the presence of external magnetic fields. An adiabatic eigenstate $|\Psi_{\rm rot}\rangle$, transformed to the laboratory frame and rotated by $\mathbf{M}(\alpha, \beta)$, leads to spectral decompositions of the measured signals.

For Faraday rotation, this is given by

$$\langle \hat{S}'_x(t) \rangle = -\frac{1}{2} G_F^{(1)} S_y n_F \hbar F_z \sum_{n=0}^{1} \tilde{h}_n(\theta) e^{in\omega t} + \text{c.c.}, \quad (8)$$

using $\langle F, F_z | \hat{F}_z | F, F_z \rangle = \hbar F_z$. From Eqs. (A10) and (A11), we find the spectral components in the small angle approximation

$$(\tilde{h}_0, \tilde{h}_1)^T(\theta) \approx \begin{pmatrix} \cos\theta \\ (\beta \pm i\alpha)\sin\theta \end{pmatrix}, \quad (9)$$

for $\alpha, \beta \ll 1$, i.e., for $B_{x,y} \ll B_z$. The principal behavior of these functions across rf resonance is depicted in Fig. 2(a). This spectral decomposition shows rf-resonant behavior. The transverse field components are mapped onto the quadratures of the first harmonic according to $\beta \pm i\alpha \approx (B_x \mp iB_y)/B_z$ and with an oscillation amplitude proportional to $\sin\theta$. The latter is maximal for $\theta = \pi/2$, i.e., exactly on rf resonance. At the same time, the zeroth harmonic, i.e., the dc signal, exhibits dispersive behavior that maps the total static field strength, which is proportional to B_z in the first-order approximation near resonance. This configuration represents a vector magnetometer, but the dc component of the signal is quite vulnerable to electronic and technical noise, which will limit this strategy in practice to sensitive measurements of only the two transverse field components.

When measuring the Voigt effect, the spectral decomposition of the signal leads up to the second harmonic and is given by

$$\langle \hat{S}'_z(t) \rangle = \frac{1}{2} G_F^{(2)} S_y n_F \hbar^2 \xi_F(F_z) \sum_{n=0}^{2} h_n(\theta) e^{in\omega t} + \text{c.c.}, \quad (10)$$

using $\langle F, F_z | \hat{F}_y^2 - \hat{F}_z^2 | F, F_z \rangle = \hbar^2 (F(F+1) - 3F_z^2)/2 = \hbar^2 \xi_F(F_z)$.

According to Eqs. (A13)–(A15), the spectral components in the small-angle approximation are in this case

$$(h_0, h_1, h_2)^T(\theta) \approx \begin{pmatrix} 0 \\ (\beta \mp i\alpha)\sin 2\theta \\ -\sin^2\theta \end{pmatrix}. \quad (11)$$

The principal behavior of these functions is shown in Fig. 2(b). Again, the transverse field components are mapped onto the quadratures of the first harmonic, but now with a dispersive shape given by an oscillation amplitude proportional to $\sin 2\theta$. Maximal amplitude is reached at $\theta = \pi/4$ and $3\pi/4$, i.e., when the static field is $B_{\rm dc} = B^{\pm}_{\rm sense} = B_{\rm res} \pm B_\rho$. In contrast to the Faraday decomposition, the zeroth harmonic vanishes while the second harmonic depends on the static field amplitude. Conveniently, the maximum sensitivity and approximately linear response to B_z are also met at $B_{\rm dc} = B^{\pm}_{\rm sense}$. Hence, the Voigt rotation enables low-noise detection of all three magnetic components by evaluating the first and second signal harmonics. For the Voigt-effect measurements presented in the following, we work on the high-field side of the rf resonance, by applying a field in the z direction of strength $B_{\rm offs} = B^{+}_{\rm sense}(\alpha = \beta = 0) = B_{\rm res} + B_{\rm rf}/2$. At this setting, the explicit second-order expansion of the three relevant signal quadratures is given by

$$\text{Re}(h_1) = h_x = +\left(\frac{1}{B_{\rm offs}} - \frac{\delta B_z}{B_{\rm offs}^2}\right) B_x, \quad (12)$$

$$\text{Im}(h_1) = h_y = -\left(\frac{1}{B_{\rm offs}} - \frac{\delta B_z}{B_{\rm offs}^2}\right) B_y, \quad (13)$$

$$\text{Re}(h_2) = h_z = -\frac{1}{2} + \frac{\delta B_z}{B_{\rm rf}} - \left(\frac{\delta B_z}{B_{\rm rf}}\right)^2 + \frac{2B_{\rm offs} + B_{\rm rf}}{4B_{\rm offs}^2 B_{\rm rf}} B_x^2 + \frac{B_{\rm offs} + B_{\rm rf}}{2B_{\rm offs}^2 B_{\rm rf}} B_y^2. \quad (14)$$

III. EXPERIMENTAL REALIZATION: LASER COOLED ATOMS

A. Laser cooled atoms setup

Our experimental cold atom setup, see Fig. 3, was described in [19], and here we will present only a brief description. We prepare an ensemble of approximately 2×10^7 laser cooled ^{87}Rb atoms with a temperature of $(80 \pm 10)\,\mu$K in the $|F = 2, m_F = 0\rangle$ state, using a sequence of optical pumping and state cleaning steps. Here, optical pump light propagating along a second optical axis was used to simplify the state preparation. Atoms are then adiabatically dressed with a magnetic rf field in the x direction with frequency

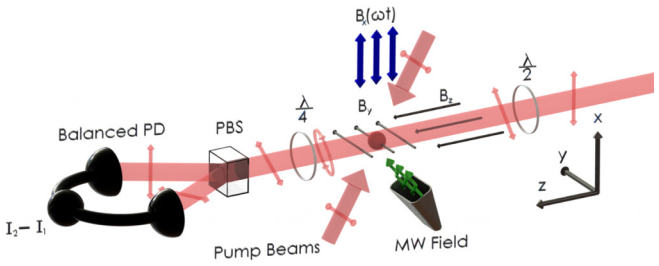

FIG. 3. Experimental setup. A laser cooled ^{87}Rb sample is prepared in a pure $|F = 2, F_y = 0\rangle$ state. After rotation of the static field into the z direction and adiabatic dressing with a magnetic rf field along x, linear birefringence of the sample is probed polarimetrically by a laser pulse propagating along z.

$\omega = 2\pi \times 180$ kHz, generated by an external resonant coil. The rf field amplitude is ramped up to ≈15 mG over 4 ms while the static magnetic field is ramped to a magnitude of $B_{\text{offs}} \approx 260$ mG along the z direction, which tunes the atomic Larmor frequency near resonance.

We measure the Voigt effect with a laser beam ($P \approx 100\,\mu$W, $\oslash \approx 2.5$ mm) detuned by -400 MHz from the $F = 2 \rightarrow F' = 2$ transition of the ^{87}Rb-D_1 line. A half-waveplate sets the polarization at 45° with respect to the x and y axes. After interaction of a 1-ms-long probe pulse with the ensemble, a quarter-waveplate and a Wollaston prism allow us to measure the linear birefringence of the medium. The light is detected on a balanced photodetector pair (Thorlabs PDB210A) with a high-pass filtering rf amplifier (Minicircuits Model ZFL-1000+). The output voltage u is proportional to the observed ellipticity, i.e., $u(t) = g_{\text{el}} S'_z(t)$ with electronic gain g_{el}, on the order of 10^{-12} V/Hz. The output signal is acquired by a field programmable gate array (FPGA) and is demodulated digitally with reference to the phase of the rf field.

B. Field mapping with laser cooled atoms

The atomic ensemble should operate as a vector magnetometer near $\mathbf{B} = B^{+}_{\text{sense}}\mathbf{e}_z$, where the two frequency modes of the atomic response map the three components of the magnetic field. Detuned to one half width at half maximum above the rf resonance, the signal amplitude at 2ω will be sensitive to the longitudinal field, while the two quadratures of the signal amplitude at ω map the transverse fields.

Figure 4 shows experimental signals demodulated at frequencies ω and 2ω as a function of the static field $B_z\mathbf{e}_z$ (see more details in Sec. IV E). The detected oscillation amplitude at frequency 2ω shows resonant behavior. The dispersive responses at frequency ω are observed due to the presence of a transverse field with nonzero x and y components. On the high-field side, these signals show maximal amplitude near $B_z = B^{+}_{\text{sense}} \approx 0.258$ G, where the 2ω amplitude shows an approximately linear response with respect to B_z. To show vector magnetometer operation, we scan the transverse fields in a gridlike pattern at constant B_z near the sensitive point. The results are shown in Fig. 5, together with the matching theoretical response.

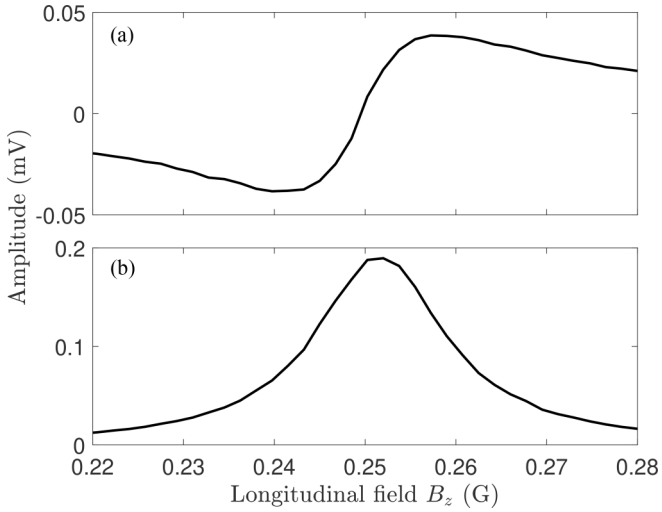

FIG. 4. Voigt-effect measurement across rf resonance. Typical experimental amplitudes of the signal harmonics. Here, in-phase components of ac voltage amplitudes oscillating at ω (a) and at 2ω (b) vary when the field component B_z is scanned across the rf resonance in the presence of a constant nonzero transverse field.

The results confirm the principle of operation for the magnetometer based on the Voigt effect in cold atoms, with well-controlled preparation of pure quantum states and temporal separation of state preparation and exposure to an external field. For practical purposes, this setup is of limited use, given the complexity of the apparatus and limitations on achievable sample proximity and bandwidth or cycle rate.

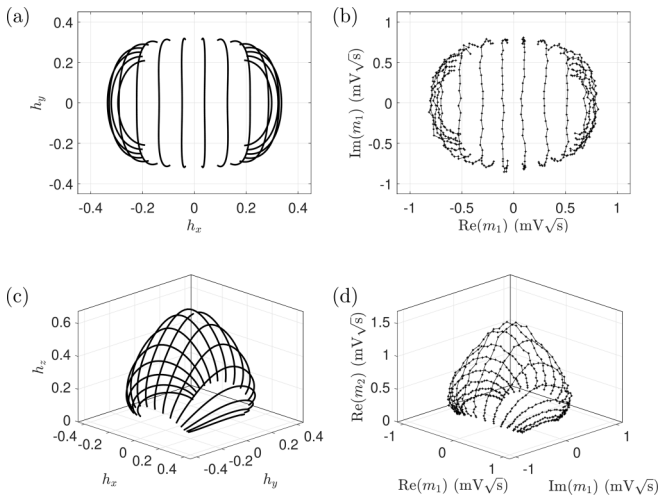

FIG. 5. Atomic response, mapping the external magnetic-field vector onto harmonic signal components. (a) Theoretical response of the signal quadratures at frequency ω, as a function of the transverse field components B_x and B_y for constant B_z. (b) Full three-dimensional response (see the Appendix), including the real part of the signal amplitude at frequency 2ω, which allows for the measurement of the longitudinal field B_z. (c) Experimental realization, showing real and imaginary parts of the complex signal amplitude m_1 (detailed description in Sec. IV E) at ω as a function of scanned transverse fields. The separation between two vertical lines is $\Delta B_x \approx 9$ mG. (d) Full experimental response of both amplitudes m_1 and m_2 as a function of the scanned field.

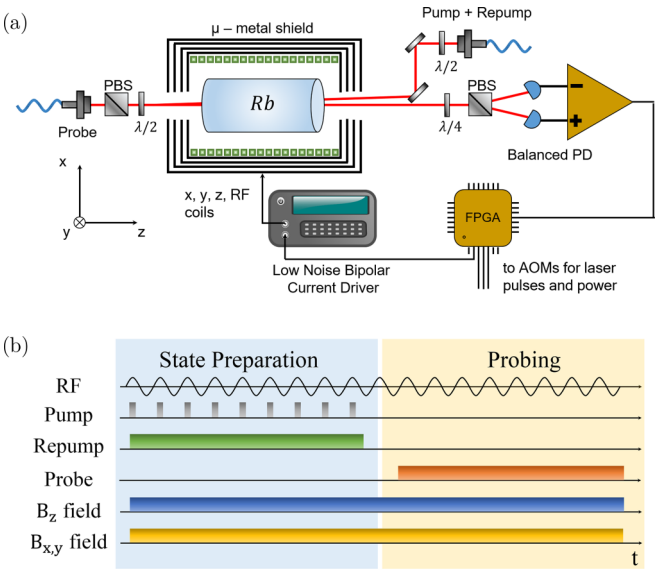

FIG. 6. Experimental realization with a shielded vapor cell. (a) Layout of the experimental setup. A pair of pump beams is used to prepare the atomic state before a polarimetric measurement is performed on a counterpropagating probe beam. The pump light is incident under a small angle with respect to the probe and the static offset field. (b) Single shot experimental pulse sequence with a typical 8-ms duration. During each cycle, the static fields are held at constant scanned values after switching within $\leqslant 50\,\mu$s at the start of the state preparation process.

Therefore, we explored Voigt-effect magnetometry in a vapor cell with room-temperature atoms towards practical devices with higher bandwidth and sensitivity.

IV. EXPERIMENTAL REALIZATION: ROOM-TEMPERATURE VAPOR

A. Room-temperature vapor setup

Our setup is based on a paraffin coated ^{87}Rb enriched vapor cell of diameter $d = 26$ mm and length $l = 106$ mm at room temperature, with a density of approximately 10^{10} atoms per cubic cm. The cell is placed inside a commercial four-layer μ-metal shield (Twinleaf MS-2), mounted on a nonmagnetic vibration isolation table with nonmagnetic optomechanics [see Fig. 6(a)]. The static magnetic fields and the radio-frequency field inside the chamber are generated by a combination of a solenoid for the longitudinal field and cosine-theta coils for the transversal fields. The coils are driven by a lead-acid battery powered, ultra-low-noise current sources, based on the modified Hall-Librecht design [24,25]. The laser system to address the atomic transitions for state preparation and probing consists of a combination of commercial and in-house external cavity diode lasers. The laser system is housed on a separate vibration isolation table, and the light is coupled via single-mode polarization maintaining fibers.

The atomic vapor is optically pumped with a linearly polarized pair of laser beams, counterpropagating to a linearly polarized probe beam. A small angle is used for optical access. The Voigt rotation is measured by separating the two circular polarization components with a quarter-waveplate and polarizer cube and detecting the light with a balanced photodetector pair (Thorlabs PDB210A), with electronic gain $g_{\rm el} \approx 10^{-13}$ V/Hz. The magnetometer is operated in pump-probe mode, where each cycle contains an initial period of synchronous optical pumping before probing the atomic state. The experimental sequence generation and data acquisition are performed using a National Instruments FPGA (PCIe-7852).

B. State preparation

In each cycle, we perform the state preparation by optical pumping, which reaches a steady state over the first 5 ms, before probing the state for another 3 ms [see Fig. 6(b)]. However, different from the cold atom test case, the magnetic fields are not adiabatically ramped to different values between pump and probe stages. Here, we prepare dressed states directly by synchronous pumping [26], i.e., using a pulse train of pump light, in phase with a uniform 5-kHz rf field of $\lessapprox 0.1$ mG, near resonant with the static field B_z. We use linear polarization along the x axis, parallel to the rf field. During a short 9% duty cycle, this direction is nearly aligned with our quantization axis in the rotating frame. This enables the preparation of either the dressed state $|F = 2, m_F = 0\rangle$ for pumping near the $F = 2 \rightarrow F' = 2$ transition on the D_1 line or an incoherent mixture of $|F = 2, m_F = \pm 2\rangle$ for pumping near $F = 2 \rightarrow F' = 1$. Our signal amplitude depends quadratically on the magnetic quantum number m, and all three of these states give rise to the same maximally possible signal with $\xi_F(2) = \xi_F(-2) = -\xi_F(0)$. The choice of states and required pump polarization allows for the pump beam to propagate parallel to the probe beam, along the z axis.

To maximize atomic population in the $F = 2$-hyperfine manifold, a copropagating CW repump beam addressing $|F = 1\rangle \rightarrow |F' = 2\rangle$ of the D2 line of the same polarization is spatially overlapped with the pump, which repopulates atoms from the $|F = 1\rangle$ to the $|F = 2\rangle$ ground state. The pump and repump beams share the same Gaussian intensity profile with 7.3-mm diameter ($1/e^2$) and 2.2- and 1.6-mW/cm^2 peak intensity, respectively. The pumping efficiency is limited by atom exchange, spin-exchange collisions, other decoherence processes, nonparallel effective field and pump polarization at the sensitive field offset $B^+_{\rm sense}$ where $\theta = \pi/4$, and the synchronized pump duty cycle, which is a compromise between effective power and achieving momentary alignment between effective field and polarization. The resulting spin state can be characterized spectroscopically [28], and here we used a stroboscopic version of microwave spectroscopy to probe the dressed atomic states [29]. The experimental lower estimate confirmed that more than 75% of the atomic population is pumped into a mixture of the dressed states $|F = 2, m = \pm 2\rangle$. Details of this method will be published elsewhere. The imperfect pumping efficiency reduces the overall signal strength due to a reduction of the atomic alignment but may also influence collisional dynamics at sufficiently high atomic densities.

C. Signal detection

Immediately after the state preparation process we couple a counterpropagating probe pulse along z to measure the

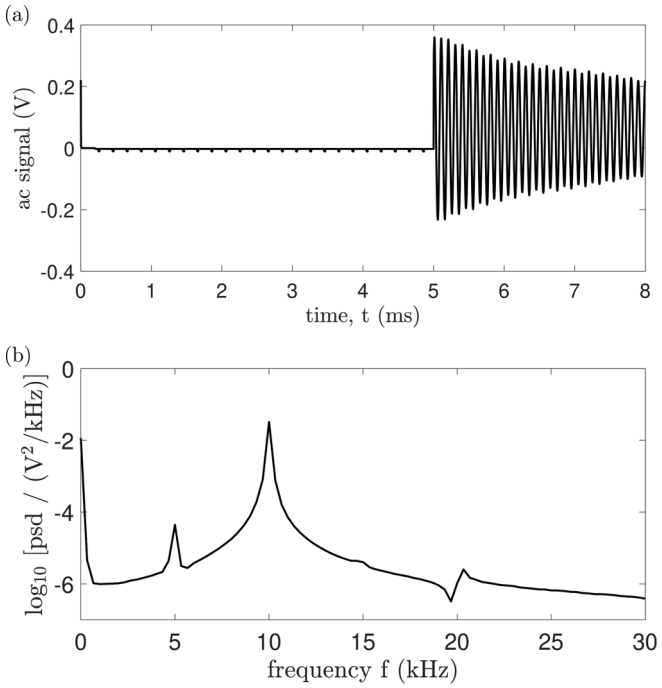

FIG. 7. Typical experimental signals. (a) Raw balanced signal of the Voigt rotation. The state preparation occurs within the first 5 ms of the cycle followed by a 3-ms probing pulse. (b) Single-sided power spectral density (psd) of the amplified signal during the probe pulse. Atomic signals arise at ω and 2ω. Weak harmonics at 3ω and 4ω can also be observed, which may arise due to nonlinear magneto-optical effects [27] and nonlinearities in the electronic detection path. For comparison, photon shot noise is at a level of $g_{\mathrm{el}}^2 S_y \approx 0.6 \times 10^{-10}\,\mathrm{V}^2/\mathrm{kHz}$.

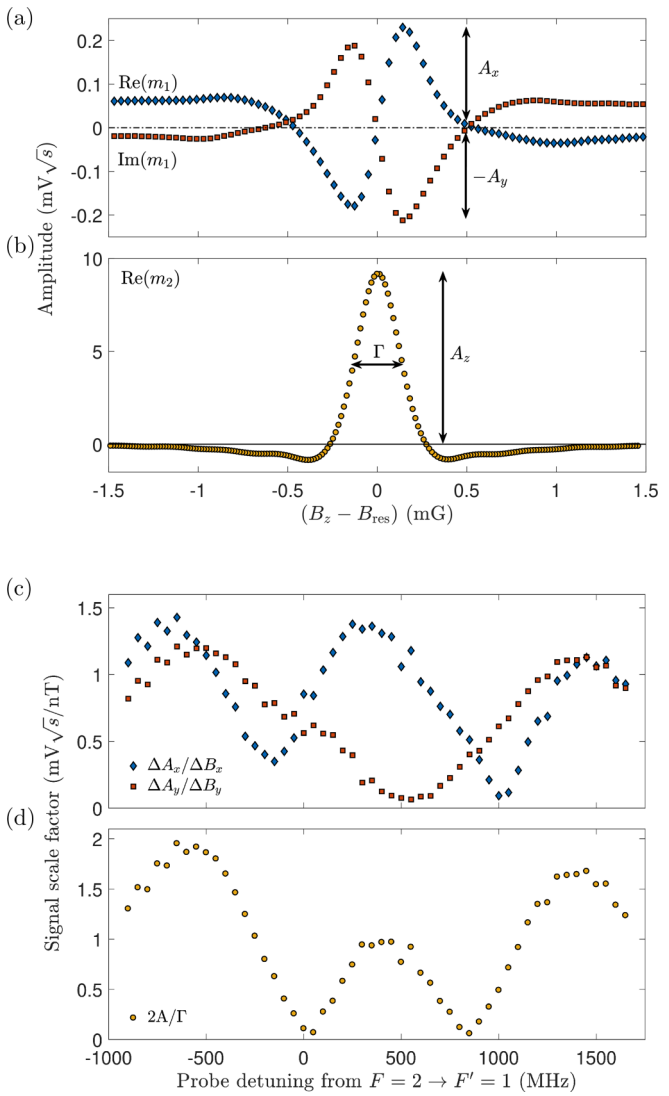

FIG. 8. Experimental magnetometer response. (a, b) The three relevant quadratures of the mode amplitudes m_1 and m_2, i.e., responses at frequencies ω and 2ω, for a scan of the longitudinal field B_z across the rf resonance. Here, nonzero transverse fields B_x and B_y are kept constant. The mode amplitudes, extracted according to Eq. (15), follow the predicted behavior [see Eq. (7)]. (c, d) Experimental estimates for the three signal scale factors as a function of probe detuning. For the longitudinal field, this is the slope of the 2ω resonance profile, estimated as $2A/\Gamma$. Near the chosen probe detuning of -550 MHz, all scale factors are close to maximal, and the first-order responses to orthogonal external fields are orthogonal.

resultant Voigt rotation. The probe is detuned by -550 MHz from the $|F = 2\rangle \rightarrow |F' = 1\rangle$ transition of the D1 line. It has a Gaussian profile of 3.4-mm diameter ($1/e^2$) and 2.6-mW/cm^2 peak intensity and linear polarization set to 45° with respect to the rf field.

The interaction with the dressed atomic medium results in modulated elliptical polarization of the probe. Figure 7 shows the typical temporal trace of the balanced detector signal during one cycle together with its spectrum. The main contributions to the rf signal are found at frequency $2\omega = 10$ kHz and a weaker signal at the dressing frequency $\omega = 5$ kHz due to the presence of transverse fields. As can be seen in Fig. 7(a), the atomic signal decays due to finite state lifetime. Generally, this is limited by the atom-wall and atom-atom collision rates. In our case, the exchange of the atoms between the main cell body and the stem with the Rb reservoir is the major contributing factor to the relaxation rate. In principle, high-quality antirelaxation coatings together with a lockable stem system can be used to achieve coherence lifetimes in excess of 60 s [30].

Absorption of the probe beam introduces additional decay and additional optical pumping, which broadens the 2ω resonance profile and alters the response at ω to transverse fields. We choose the combination of probe power and detuning by optimizing the slope of the 2ω signal with respect to the external field strength. We evaluate this scale factor as the ratio of height A_z and width $\Gamma/2$ of the resonance peak, both indicated in Fig. 8(b). The dependence on probe detuning is shown in Fig. 8(d). The maximal response to longitudinal fields is found away from the Doppler broadened absorption lines, where also the signal responses to small changes of the two orthogonal transverse field components are close to maximal, shown in Fig. 8(a), and show the predicted $\pi/2$ relative phase shift. Closer to the resonances, we observe different and nonorthogonal responses.

The detected raw signals are digitally demodulated to extract the three-dimensional field vector information. We

calculate complex temporal mode amplitudes m_k for the first and second harmonic ($k = 1, 2$) by taking the scalar product of the signal $u(t) = g_{\rm el} S_z'(t)$ with exponentially decaying normalized mode functions leading to the definition

$$m_k = \int_{t_1}^{t_2} e^{(-ik\omega-\gamma)t} u(t) dt \Big/ \sqrt{\int_{t_1}^{t_2} e^{-2\gamma t} dt}, \qquad (15)$$

which covers the interval of the probe pulse between times t_1 and t_2 and matches the atomic response. To first order and for appropriately adjusted phase, the quadratures, i.e., the real and imaginary part of m_1, reflect the external field components B_x and B_y while the real m_2 is sensitive to B_z. The signals are phase locked to the rf driving field, but they acquire additional electronic phase shifts. Therefore, we first adjust the demodulation phase for the second-harmonic signal by scanning the longitudinal B_z field while the transverse fields are set to zero. We adjust the phase such that the real and imaginary quadratures of the mode amplitude m_2 produce a symmetric and a dispersive profile, respectively. Any additional phase entering the first harmonic is equivalent to a rotation of the field coordinate system about the longitudinal axis. Here, we scan the transverse fields over a small range, with the longitudinal field adjusted to the sensitive field point $B_z \approx B^+_{\rm sense}$ to identify two orthogonal quadratures with the x- and y-transverse field coils by minimizing their crosstalk. As it is shown in Fig. 8(a) both quadratures of the signal amplitude m_1 follow a dispersive profile. Figure 8(b) shows the resonant response of the amplitude $\mathrm{Re}(m_2)$. This is consistent with the theoretical model described in Sec. II and with the experimental results for cold atoms in Sec. III B. In contrast to the double resonance magnetometer described in [20], where the quadratures of the first harmonic present a resonant and a dispersive profile with respect to the applied static field, the quadratures in Fig. 8(a) are both dispersive while one quadrature of the second harmonic shows a resonant profile. All three signals become most sensitive to orthogonal external field components at the same offset field.

The conversion of measured signals into magnetic-field values relies on a two-step calibration procedure. First, the static field coils are characterized with two independent methods, before the signal scale factor for each field direction is determined by applying a range of known fields to the magnetometer. The static field coils together with their electronic drivers are calibrated using the known field dependence of the Larmor resonance for ^{87}rubidium. For a set of fixed radio frequencies ω, the longitudinal field B_z is scanned with no transverse fields present to find the maximal response of the 2ω signal. Under this condition, the field is determined by known parameters according to $B_z = B_{\rm res} = \hbar\omega/\mu_B|g_F|$. The resonant field can be easily calculated and plotted against the applied voltage per current of the coils giving the field conversion. The presence of transverse fields changes the resonance condition to $B_{\rm res} = \hbar\omega/\mu_B|g_F|\sqrt{B_z^2 + B_{x,y}^2}$. Thus, to obtain the calibration for the transverse fields, we change one of the transverse fields while keeping the other one at zero and sweep the B_z field to obtain a new location of the 2ω resonance. As before, the new resonance location is evaluated as a function of the control voltage per current of the coils. In addition to this procedure, we confirm the coil calibrations using a commercial fluxgate magnetometer (Stefan Mayer Instruments, FLC3-70). Finally, the signal scale factors are measured by applying a linear field ramp of a well-known range to each of the fields independently. For small fields, the corresponding demodulated signal responses show linear relationships [see Eqs. (12)–(14)], which we use to calibrate the signal-to-field conversion.

D. 3D vector mapping

Following the same procedure as in the cold atom case in Sec. III B, we measured the three components of the field by setting the static field $B_z = B_{\rm sense}$, which maximizes the mode amplitudes at ω. By linearly scanning the external transverse fields and demodulating the ω and 2ω quadratures, we are able to map the magnetometer response. The vector magnetometer operation can be visualized on a 3D plot shown in Fig. 9. The full mathematical description of the oviform plot can be found in the Appendix, but it must be noted that the theoretical results are based on the assumption of a pure atomic state. The model does not account for decoherence due to atomic collisions and various broadening effects (e.g., gradient fields and light power). Nevertheless, the experimental results are in reasonable agreement with the expected three-dimensional response [see Eqs. (12)–(14)]. As can be seen in Fig. 9 the two-dimensional and 3D oviform profiles arising from magnetic-field scans show some asymmetric distortion and an offset, which arise from geometrical misalignment of the probe and pump beams relative to the static fields and/or the rf dressing field as confirmed for larger misalignment. The insets show the magnetometer response in the linear regime for small external fields.

Despite the theoretical simplifications, our model effectively describes the vector magnetometer response to the external magnetic fields. We assume that effects of distortion can be reduced by accurate alignment between the probe and pump beams, the dressing field, and the small static offset fields. Operation at higher dressing frequency and thus larger offset field leads to more accurate alignment of the field across the atomic ensemble; however, this method reduces the sensitivity to the transverse fields as described in the following section. The sensing range for the longitudinal field is determined by the width of the resonance, while the response to transverse fields and its nonlinearity is determined by their ratio to the offset field. In principle, the range of operation can be extended and maximal sensitivity maintained by placing the magnetometer into a closed-loop system.

E. Noise performance

To perform the noise measurements we detune the static B_z field to $B_z = B^+_{\rm sense}$, which optimizes the magnetometer sensitivity for all three components. We then adjust the transverse fields such that the first-harmonic signal vanishes, i.e., the noise measurements are done near the apex of the middle (blue) ovoid in Fig. 9(b).

Based on the field calibrations described above, we record field equivalent signal noise for the three field components over ≈16 s (2048 cycles at 125 Hz). Figure 10 shows the spectral noise performance for the two quadratures at ω and

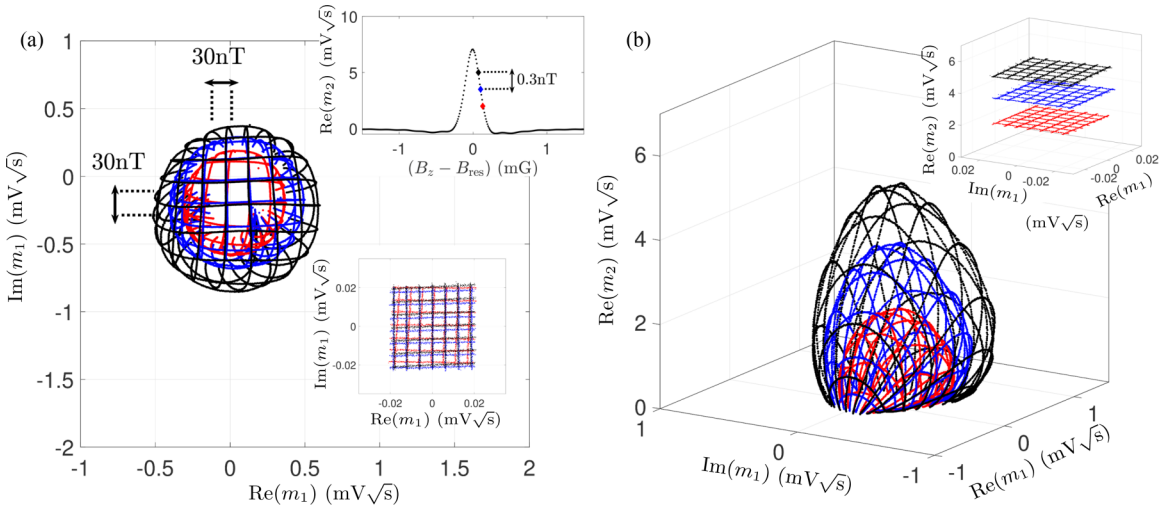

FIG. 9. Mapping of the OPM response to external fields at 5-kHz radio-frequency dressing. (a) Quadratures of the first-harmonic signal as a function of raster scanned transverse fields $B_{x,y}$ ranging over $\approx\pm180$ nT for constant B_z. Each color represents a different B_z field ranging over $\approx\pm0.3$ nT. The top inset shows the location of the B_z field with respect to the resonant signal at 2ω. (b) Inclusion of the second-harmonic signal produces oviforms in the three-dimensional representation and demonstrates the full vector mapping. The behavior in the linear regime for small field perturbations is shown in the insets, with visible photon shot noise $g_{\mathrm{el}}\sqrt{S_y} \approx 2.5 \times 10^{-4}$ mV$\sqrt{\mathrm{s}}$. We attribute deviations from the ideal profiles to geometric misalignment between the pump and probe beams and static and rf fields. The asymmetric distortion increases for lower-bias fields, consistent with imperfect orthogonality between static field coils and their alignment with the direction of the probe beam.

the in-phase quadrature at 2ω. At 5-kHz rf dressing frequency and a temperature of 36 °C, the magnetometer operates with an average noise level of $\approx$2.2 pT/$\sqrt{\mathrm{Hz}}$ for the transverse fields over the range of 10–62.5 Hz, dominated by photon shot noise. Longitudinal fields can be measured with a sensitivity of 0.4 pT/$\sqrt{\mathrm{Hz}}$. The dominant constraint on the noise level is the short coherence time of the cell ($\tau \approx 2$ ms) which is limited by the quality of the paraffin coating and the exchange of the atoms between the main cell body and the stem with the Rb reservoir. Typically, paraffin or OTS coated cells have coherence times ranging from 30 to 300 ms [31,32]. Longer coherence time would improve the field sensitivity of the OPM due to a larger fraction of atoms remaining in the field sensitive state. In addition, higher-quality paraffin coating would also shorten the pump and repump pulse time needed to (re-)prepare the stretched states, allowing for increased cycle rate and thus higher bandwidth as well as higher duty cycle and thus reduced aliasing of magnetic-field noise.

We have investigated the effects of heating the cell to increase the atomic density, which should in principle improve the sensitivity by increasing signal strength. However, as it is shown in Fig. 11(a), the signal-to-noise ratio saturates already at temperatures of approximately 32 °C for the transverse fields and at even lower temperatures for the longitudinal fields. Initially, increasing signal amplitudes lead to better sensitivity, especially for the transverse fields where the signals are closer to photon shot noise, but additional atomic processes such as resonance broadening limit the performance at higher temperature where the figure of merit saturates. A similar saturation effect was previously observed in [33], where higher atomic concentrations lead to an increase of the collisional and surface relaxation rates, depolarizing the prepared state.

The sensitivity of the OPM to transverse fields depends not only on the shape of the resonance but also on the chosen dressing frequency, because the corresponding signals arise from the geometric rotation of the static field. The rotation angle and consequently the signal strength increase for smaller offset fields [see Eqs. (12) and (13)]. The resulting linear dependence of sensitivity on dressing frequency is shown in Fig. 11(b). Over the range of 40 to 2.5 kHz the transverse field noise performance varies by a factor of 4. This strategy is limited by the linewidth of the rf resonance and other factors such as the required precision of alignment increased susceptibility to magnetic-field gradients distorting the oviform mapping.

V. CONCLUSIONS

We have presented and successfully demonstrated a full vector magnetometer based on the Voigt effect both in cold atom and hot vapor setups. As shown, our scheme has the advantage of requiring only a single optical axis for state preparation and detection, making it ideal for compact magnetic-field sensors. We have achieved pT/$\sqrt{\mathrm{Hz}}$ sensitivity with a 62.5-Hz bandwidth. Our current limitations in the sensitivity of the OPM stem from the coherence time of the cell and the low atom number. Future improvements will include a heated and buffer gas filled cell in order to increase the atom numbers and reduce the rate of atomic collisions that induce decoherence effects, respectively. These improvements should shorten the state preparation lifetime, thus increasing the bandwidth and the field sensitivity of the OPM. In principle, placing the cell in an optical resonator may be used to increase the interaction path between the light and the atoms, thus further improving the sensitivity.

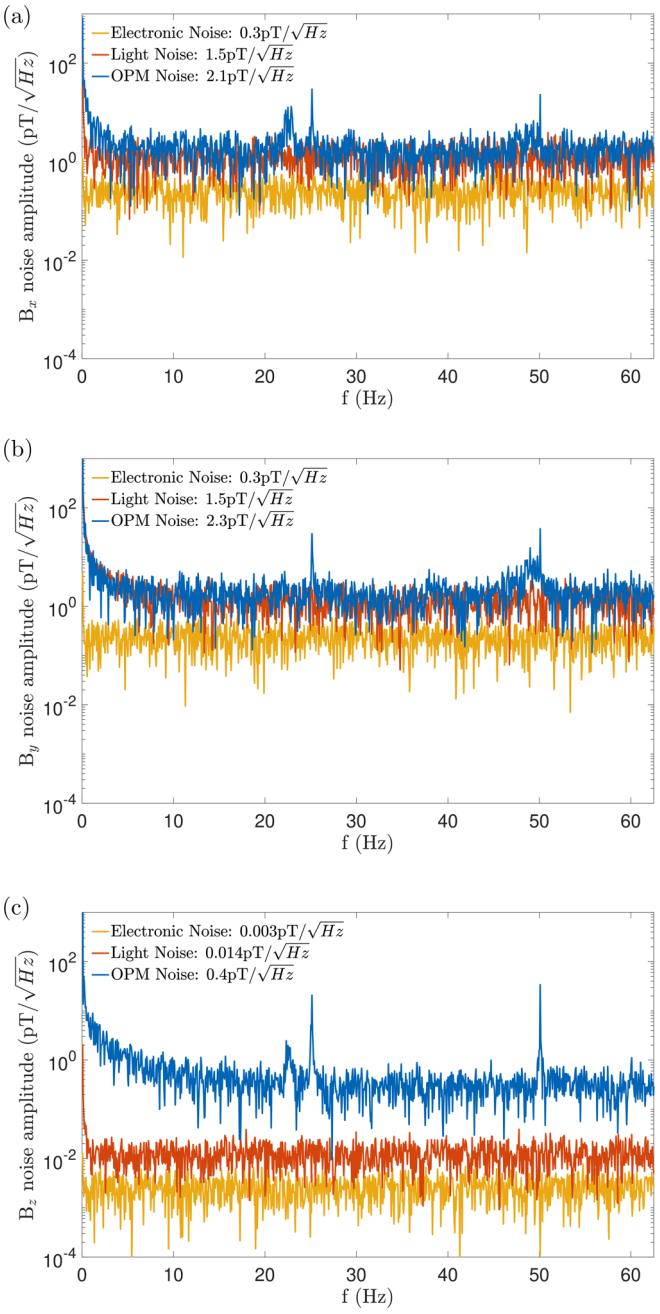

FIG. 10. OPM noise at 36 °C vapor cell temperature in a shielded environment at 5-kHz radio-frequency dressing. Noise floor values are estimated for the range 10–62.5 Hz. (a, b) Noise performance for the two orthogonal transverse fields. The light noise in one of the signal quadratures shows phase-locked low-frequency fluctuations of cross talk between the rf generation and detection paths. (c) Noise performance for the longitudinal field component. The light noise levels (photon shot noise) are obtained with a far-detuned probe laser and disabled pump and repump lasers. The electronic noise is recorded without probe light and no rf field present. The calibration of field equivalent noise amplitudes includes an ≈5% drop of the low-pass frequency response function, which is predominantly determined by the mode function entering Eq. (15).

The datasets generated for this paper are accessible at [34] Nottingham Research Data Management Repository.

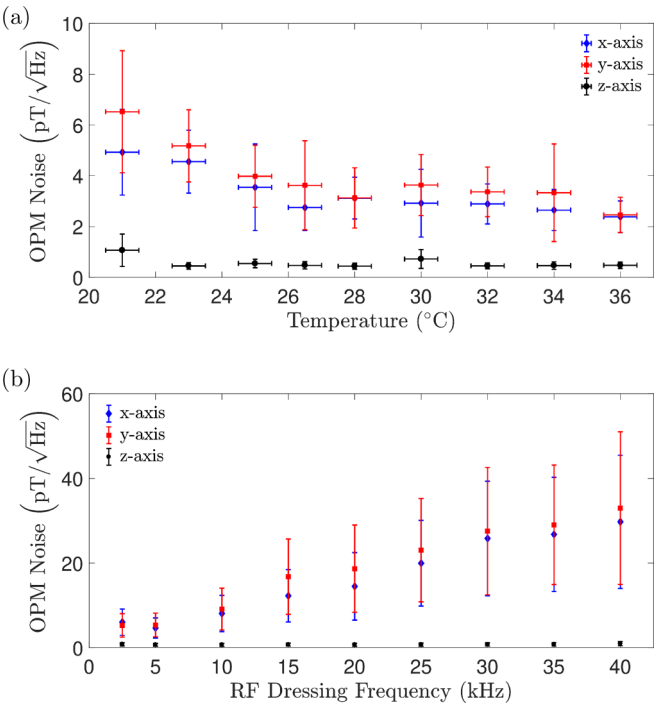

FIG. 11. Dependencies of the noise performance. (a) OPM noise as a function of the vapor cell temperature. (b) OPM noise as a function of radio frequency of the dressing field.

ACKNOWLEDGMENTS

This work was funded by the UK Engineering and Physical Sciences Research Council (EPSRC) Grant No. EP/M013294/1. We acknowledge support from the School of Physics and Astronomy Engineering and Electronics workshops. We thank Sindhu Jammi for collecting the cold atoms data. We thank Konstantinos Poulios and Kasper Jensen for useful discussions.

APPENDIX: FARADAY AND VOIGT ROTATION FOR DRESSED STATES

In what follows we present a brief description of the atom dynamics and the resulting behavior of Faraday and Voigt rotation, following [19].

Starting from our effective rotating frame Hamiltonian in Eq. (1), the dressed states are of the form

$$|\Psi_{\rm rot}\rangle = e^{i\theta \hat{F}_y/\hbar}|F, F_z\rangle, \tag{A1}$$

where θ is the angle of the effective magnetic-field direction, given in Eq. (2). In the laboratory frame, the same states are given by

$$|\Psi(t)\rangle = \hat{U}_{\pm}^{-1}(t)|\Psi_{\rm rot}\rangle, \tag{A2}$$

where $\hat{U}_{\pm}(t) = e^{\pm i\omega t \hat{F}_z/\hbar}$. Combining the two rotation operators, the expectation value of any laboratory frame atomic observable can be expressed as

$$\langle\Psi(t)|\hat{O}|\Psi(t)\rangle = \langle F, F_z|\hat{R}_{\pm}\hat{O}\hat{R}_{\pm}^{-1}|F, F_z\rangle, \tag{A3}$$

$$\hat{R}_{\pm}(t) = e^{-i\theta \hat{F}_y/\hbar}\hat{U}_{\pm}(t). \tag{A4}$$

Using the Baker-Hausdorff lemma

$$e^{\hat{A}}\hat{B}e^{-\hat{A}} = \hat{B} + [\hat{A},\hat{B}] + \frac{1}{2!}[\hat{A},[\hat{A},\hat{B}]] + \ldots, \tag{A5}$$

it can be shown that for a Cartesian vector operator the corresponding Heisenberg operator is given by a geometric rotation, i.e.,

$$\hat{\mathbf{O}}'(t) = \hat{R}_{\pm}(t)\hat{\mathbf{O}}\hat{R}_{\pm}^{-1}(t) = \mathbf{R}_{\pm}(t)\hat{\mathbf{O}}, \tag{A6}$$

where $\mathbf{R}_{\pm}(t) = \mathbf{R_z}(\pm\omega t)\mathbf{R_y}(-\theta)$ [23]. Including the rotations of the static field as shown in Fig. 1, such that $\hat{\mathbf{F}}'(t) = \mathbf{M}(\alpha,\beta)\hat{\mathbf{R}}_{\pm}(t)\hat{\mathbf{F}}$, we find an expression for the longitudinal spin component

$$\begin{aligned}\langle\hat{F}_z'(t)\rangle = {} & \langle\hat{F}_x\rangle[c_\alpha c_\beta s_\theta - c_\theta(c_{\omega t}s_\beta + c_\beta s_\alpha s_{\omega t})] \\ & + \langle\hat{F}_y\rangle(c_\beta c_{\omega t}s_\alpha - s_\beta s_{\omega t}) \\ & + \langle\hat{F}_z\rangle[c_\alpha c_\beta c_\theta + s_\theta(c_{\omega t}s_\beta + c_\beta s_\alpha s_{\omega t})],\end{aligned} \tag{A7}$$

where s_ν (c_ν) stands for $\sin(\nu)$ [$\cos(\nu)$] with $\nu \in \{\alpha,\beta,\omega t\}$. For the dressed states, i.e., for eigenstates of the rotating frame Hamiltonian, the relevant expectation values $\langle\hat{F}_{x,y,z}\rangle = \langle F,F_z|\hat{F}_{x,y,z}|F,F_z\rangle$ are constant, with $\langle\hat{F}_z\rangle = \hbar F_z$ and $\langle\hat{F}_{x,y}\rangle = 0$. The longitudinal spin polarization determines the Faraday rotation [see Eq. (6)], and we obtain

$$\langle\hat{S}_x'(t)\rangle = -G_F^{(1)}S_y n_F \hbar F_z[c_\alpha c_\beta c_\theta + s_\theta(c_{\omega t}s_\beta + c_\beta s_\alpha s_{\omega t})]. \tag{A8}$$

The result can be expanded in terms of spectral components as

$$\langle\hat{S}'_x(t)\rangle = -\frac{1}{2}G_F^{(1)}S_y n_F \hbar F_z \sum_{n=0}^{1}\tilde{h}_n(\theta)e^{in\omega t} + \text{c.c.}, \tag{A9}$$

where the spectral amplitudes vary as

$$\tilde{h}_0 = \cos\alpha\cos\beta\cos\theta, \tag{A10}$$

$$\tilde{h}_1 = (\sin\beta \pm i\sin\alpha\cos\beta)\sin\theta. \tag{A11}$$

Equivalently, for the Voigt rotation, in which the elliptical light polarization is given by Eq. (7), the spectral decomposition of the mean value in Eq. (A3) for the bilinear operator $\hat{\mathbf{O}}^\dagger\hat{\mathbf{O}} = \hat{F}_x^2 - \hat{F}_y^2$ is

$$\langle\hat{S}'_z(t)\rangle = \frac{1}{2}G_F^{(2)}S_y n_F \hbar^2 \xi_F(F_z)\sum_{n=0}^{2}h_n(\theta)e^{in\omega t} + \text{c.c.}, \tag{A12}$$

where the spectral amplitudes vary as

$$h_0 = \frac{1+3\cos 2\theta}{4}\left(\frac{\cos^2\beta}{2} - \frac{(3-\cos 2\beta)}{4}\cos 2\alpha\right), \tag{A13}$$

$$h_1 = \left(\frac{1}{2}\cos\alpha\sin 2\beta \mp i\frac{(3-\cos 2\beta)}{4}\sin 2\alpha\right)\sin 2\theta, \tag{A14}$$

$$\begin{aligned}h_2 = -\Bigg(&\frac{(3-\cos 2\beta)}{4}\cos^2\alpha + \frac{1}{2}\cos 2\beta \\ &\mp \frac{i}{2}\sin\alpha\sin 2\beta\Bigg)\sin^2\theta.\end{aligned} \tag{A15}$$

In order to measure an external magnetic field, we extract three quadratures from the first- and second-harmonic signals. We separate the first harmonic into real and imaginary parts, and evaluate the real part of the second harmonic. The result is given by

$$h_x = \text{Re}h_1 = \tfrac{1}{4}(3-\cos 2\beta)\sin 2\alpha\sin 2\theta, \tag{A16}$$

$$h_y = \text{Im}h_1 = \tfrac{1}{2}\cos\alpha\sin 2\beta\sin 2\theta, \tag{A17}$$

$$h_z = \text{Re}h_2 = -\tfrac{1}{4}[(3-\cos 2\beta)\cos^2\alpha + 2\cos 2\beta]\sin^2\theta. \tag{A18}$$

[1] S. A. Murthy, D. Krause, Jr., Z. L. Li, and L. R. Hunter, Phys. Rev. Lett. **63**, 965 (1989).

[2] M. V. Romalis, W. C. Griffith, J. P. Jacobs, and E. N. Fortson, Phys. Rev. Lett. **86**, 2505 (2001).

[3] D. Budker, S. K. Lamoreaux, A. O. Sushkov, and O. P. Sushkov, Phys. Rev. A **73**, 022107 (2006).

[4] H. Xia, A. Ben-Amar Baranga, D. Hoffman, and M. V. Romalis, Appl. Phys. Lett. **89**, 211104 (2006).

[5] E. Boto, N. Holmes, J. Leggett, G. Roberts, V. Shah, S. S. Meyer, L. D. Muñoz, K. J. Mullinger, T. M. Tierney, S. Bestmann, G. R. Barnes, R. Bowtell, and M. J. Brookes, Nature (London) **555**, 657 (2018).

[6] K. Jensen, R. Budvytyte, R. A. Thomas, T. Wang, A. M. Fuchs, M. V. Balabas, G. Vasilakis, L. D. Mosgaard, H. C. Stærkind, J. H. Müller, T. Heimburg, S.-P. Olesen, and E. S. Polzik, Sci. Rep. **6**, 29638 (2016).

[7] R. Fenici, D. Brisinda, and A. M. Meloni, Exp. Rev. Mol. Diagn. **5**, 291 (2005).

[8] R. Wyllie, M. Kauer, R. T. Wakai, and T. G. Walker, Opt. Lett. **37**, 2247 (2012).

[9] D. Budker and M. Romalis, Nat. Phys. **3**, 227 (2007).

[10] J. C. Allred, R. N. Lyman, T. W. Kornack, and M. V. Romalis, Phys. Rev. Lett. **89**, 130801 (2002).

[11] H. B. Dang, A. C. Maloof, and M. V. Romalis, Appl. Phys. Lett. **97**, 151110 (2010).

[12] D. Sheng, S. Li, N. Dural, and M. V. Romalis, Phys. Rev. Lett. **110**, 160802 (2013).

[13] E. B. Alexandrov, M. V. Balabas, V. N. Kulyasov, A. E. Ivanov, A. S. Pazgalev, J. L. Rasson, A. K. Vershovski, and N. N. Yakobson, Meas. Sci. Technol. **15**, 918 (2004).

[14] H. Huang, H. Dong, L. Chen, and Y. Gao, Appl. Phys. Lett. **109**, 062404 (2016).

[15] S. J. Seltzer and M. V. Romalis, Appl. Phys. Lett. **85**, 4804 (2004).

[16] B. Patton, E. Zhivun, D. C. Hovde, and D. Budker, Phys. Rev. Lett. **113**, 013001 (2014).

[17] S. J. Ingleby, C. O'Dwyer, P. F. Griffin, A. S. Arnold, and E. Riis, Phys. Rev. A **96**, 013429 (2017).

[18] H. C. Huang, H. F. Dong, X. Y. Hu, L. Chen, and Y. Gao, Appl. Phys. Lett. **107**, 182403 (2015).

[19] S. Jammi, T. Pyragius, M. G. Bason, H. M. Florez, and T. Fernholz, Phys. Rev. A **97**, 043416 (2018).

[20] A. Weis, G. Bison, and A. S. Pazgalev, Phys. Rev. A **74**, 033401 (2006).

[21] G. Di Domenico, G. Bison, S. Groeger, P. Knowles, A. S. Pazgalev, M. Rebetez, H. Saudan, and A. Weis, Phys. Rev. A **74**, 063415 (2006).

[22] M. Auzinsh, D. Budker, and S. Rochester, *Optically Polarized Atoms* (Oxford University, New York, 2010).

[23] We use rotation matrices according to Rodrigues's rotation formula $\mathbf{R}_k(\alpha)\mathbf{v} = \mathbf{e}_k(\mathbf{e}_k \cdot \mathbf{v})(1 - \cos\alpha) + \mathbf{v}\cos\alpha + \mathbf{e}_k \times \mathbf{v}\sin\alpha$.

[24] K. G. Libbrecht and J. L. Hall, Rev. Sci. Instrum. **64**, 2133 (1993).

[25] C. J. Erickson, M. Van Zijll, G. Doermann, and D. S. Durfee, Rev. Sci. Instrum. **79**, 073107 (2008).

[26] W. E. Bell and A. L. Bloom, Phys. Rev. Lett. **6**, 280 (1961).

[27] D. Budker, W. Gawlik, D. F. Kimball, S. M. Rochester, V. V. Yashchuk, and A. Weis, Rev. Mod. Phys. **74**, 1153 (2002).

[28] B. Julsgaard, J. Sherson, J. L. Sørensen, and E. S. Polzik, J. Opt. B **6**, 5 (2004).

[29] G. A. Sinuco-Leon, B. M. Garraway, H. Mas, S. Pandey, G. Vasilakis, V. Bolpasi, W. von Klitzing, B. Foxon, S. Jammi, K. Poulios, and T. Fernholz, arXiv:1904.12073.

[30] M. V. Balabas, T. Karaulanov, M. P. Ledbetter, and D. Budker, Phys. Rev. Lett. **105**, 070801 (2010).

[31] S. J. Seltzer and M. V. Romalis, J. Appl. Phys. **106**, 114905 (2009).

[32] D. Budker, D. F. Kimball, S. M. Rochester, V. V. Yashchuk, and M. Zolotorev, Phys. Rev. A **62**, 043403 (2000).

[33] S. Pustelny, A. Wojciechowski, M. Gring, M. Kotyrba, J. Zachorowski, and W. Gawlik, J. Appl. Phys. **103**, 063108 (2008).

[34] T. Pyragius, H. Marin Florez, and T. Fernholz, Data for "A Voigt effect based 3D vector magnetometer", http://dx.doi.org/10.17639/nott.6177 (2019).